

Lingnan Hu¹

Department of Mechanical Engineering, Texas A&M University, 3123 TAMU, College Station, TX 77843 e-mail: lingnan@tamu.edu

Alan Palazzolo

TEES Professor Fellow ASME Department of Mechanical Engineering, Texas A&M University, 3123 TAMU, College Station, TX 77843 e-mail: a-palazzolo@tamu.edu

Mansour Karkoub

Professor Department of Mechanical Engineering, Texas A&M University at Qatar, Doha 23874, Qatar e-mail: mansour.karkoub@qatar.tamu.edu

Suppression of Lateral and Torsional Stick-Slip Vibrations of Drillstrings With Impact and Torsional Dampers

Violent drillstring vibrations in a well should be suppressed to prevent premature failure of the drillstring parts and borehole wall and enhance the drilling process. This paper presents novel centralized impact dampers and torsional vibration dampers for lateral and torsional stick-slip vibration suppression which will function well in the harsh environment in the well due to their all-metal construction. A drillstring vibration model is used in this paper to simulate coupled lateral and torsional vibrations of the drillstring with impact and torsional dampers installed in the drill collar (DC). The high-fidelity model utilizes Timoshenko beam finite elements (FEs) and includes stress-stiffening effects to account for the gravity and axial loading effect on the transverse string stiffness. The rotational motions of the impactors result from dry friction tangential contact forces that occur when they contact the DC or sub. The tangential forces utilize a nonlinear Hertzian contact restoring force and a nonlinear, viscous contact damping force, in place of the typical coefficient of restitution (COR) model that cannot provide the required normal and tangential contact forces. The primary conclusions drawn from the simulation results are: (1) both the lateral vibration of the drillstring that is close to the bending critical speeds and the vibration induced by destabilizing forces can be suppressed by impact dampers and (2) the torsional stick-slip motion of the drillstring can be mitigated by the torsional damper. [DOI: 10.1115/1.4033640]

Introduction

Violent drillstring vibrations in a well, including torsional stick–slip and lateral whirl vibrations, may cause premature failure of tubulars and drill bits (DBs) and damage to the borehole wall. In addition, these vibrations may result in an inefficient drilling process with excessive trips to replace worn DBs. Some approaches that utilize an elastomer and viscous fluid based damper have been applied to mitigate lateral vibrations. However, typical fluid dampers vary viscosity radically with working temperature, which may lead to inefficient damping in higher temperatures (>120 $^{\circ}$ C). But this is not the primary concern in industry since there are very few high-temperature wells currently being drilled. In the harsh deep well environment exposed to oil and water (or moisture), the combined effects of oxidization, swelling, and degradation due to age and chemical reactants on the elastomer may result in the premature ineffectiveness of the elastomer damper.

As far as torsional vibration is concerned, a viable way to avoid deep well environment problems was reported by Jansen and van den Steen [1]. They proposed an active damping system above the rotary table and reduced the threshold value for stick—slip by using feedback control. Sowers et al. [2] found that a violent whirl occurring at the bit or in the bottom hole assembly (BHA) may result in large side forces at stabilizers, thereby generating high friction torques that lead to stick—slip vibrations. In such situations, they replaced the stabilizers with roller reamers to reduce the frictional drag acting at the BHA and eventually mitigate the bit whirl.

Kyllingstad and Halsey [3] used a pendulum model with a single degree-of-freedom (DOF), in which the drillstring is assumed to be suspended at the hoist/rotary table, and applied a constant Coulomb friction torque to the DB during rotating-off-bottom (ROB) or drilling-ahead (DA) to analyze its stick-slip motion. Jansen and van den Steen [1] employed a static-sliding torque model, which is similar to the Coulomb friction torque model, and divided the torque-on-bit (TOB) into static and sliding torque by assuming that the DB never rotates backward (i.e., no rolling occurs), and that the drill pipe (DP) does not come to a complete standstill. Their assumptions are helpful for understanding how the stick-slip vibration occurs though the observations in the drilling field demonstrate three different types of stick-slip vibrations, i.e., simple speed oscillation, full stick, and backward rotation. More comprehensive drillstring models that account for multiple types of stick-slip vibrations were investigated in Refs. [4] and [5].

Although the classic Coulomb (static-sliding) torque model has provided a good estimation of torsional vibrations in many cases, Dawson et al. [6] came up with a hypothesis that the torque acting on the DB undergoes a continuous and mild reduction with an increasing spin speed. Brett [7] proved by experiment that the polycrystalline diamond compact (PDC) bit has the characteristic described in Dawson's et al. hypothesis [6] and is thereby prone to cause torsional vibrations. Moreover, the lab measurements presented in his work indicated that other types of bits may have the same characteristic (torque reduction with an increase in spin speed) as the PDC bit. This velocity-dependent friction torque is analogous to the Stribeck friction model in physics. Leine et al. [8] utilized a similar torque model, in which the dry friction torque drops with a rising rotary speed, to investigate the coupled stick-slip and whirl vibrations. In accordance with Ref. [7], the Stribeck torque model is sensitive to the type of DB, the weighton-bit (WOB), the drilling condition, and even the wear of the bit.

¹Corresponding author.

Contributed by the Technical Committee on Vibration and Sound of ASME for publication in the Journal of Vibration and Acoustics. Manuscript received December 16, 2015; final manuscript received May 11, 2016; published online June 17, 2016. Assoc. Editor: John Yu.

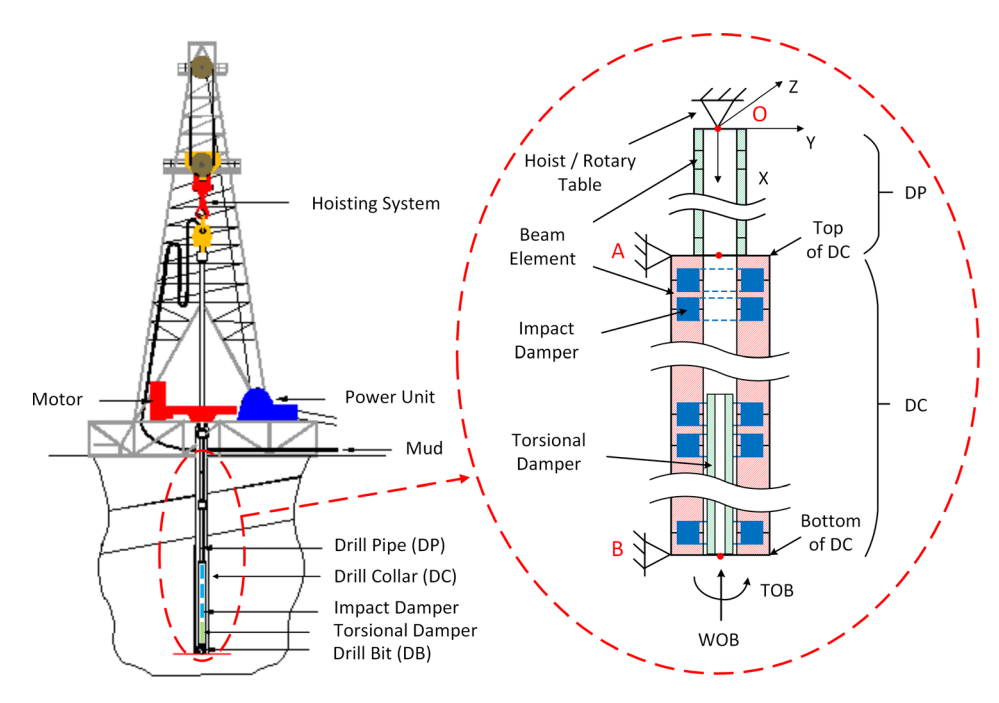


Fig. 1 Drilling rig (left) and cross section of the drillstring (right) with impact dampers and a torsional damper

With regard to the lateral whirl of a drillstring, a simplified 2DOFs lateral dynamic model of a drillstring has been presented by Jansen [9]. As stated in his paper, the lower part of a drillstring (i.e., the DC) is essential for the analysis of whirl motion, and the DC section between two stabilizers is analogous to a rotor supported by two bearings. Bailey et al. [10] used the transfer function matrices based on the Euler-Bernoulli beam bending equations to model the DC span (DC section between two nearby stabilizers). The boundary conditions were defined in two ways. One is that the DC span is pinned at both ends (stabilizers), and the other is that the span has one end built-in and the other end free. The same lateral dynamic model of a drillstring and boundary conditions was applied in Ref. [11], and the region of parameters for a DC span that contains common spin speeds, span lengths, and natural frequencies was also provided. The DC used in this paper is modeled based on this region of parameters.

Impact dampers have long been used to dampen out structural vibrations in traffic light poles, turbomachinery blades, machine tools, etc. Moore et al. [12] employed a single-DOF impacting model characterized by the COR to simulate the collision between an impact damper and an impact housing and then utilized a highspeed cryogenic rotor-bearing test rig with a multiple-impactor set that consists of impact dampers and housings to verify the simulation result that the lateral vibration was suppressed by impact dampers. McElhaney et al. [13] presented the mitigation effects of cylindrical impact dampers on lateral vibrations at resonances of a rotating shaft. The cylindrical impactor was assumed to have planar motions and impact with the housing that was connected to the shaft, but the tangential friction between the impactor and housing was neglected. The rotating shaft was modeled with multi-DOF (multiple nodes with 6DOFs per node) beam FEs. The dissipated kinetic energy was characterized by the COR.

The COR is defined as the ratio of relative translational speeds of two bodies after and before an impact. According to the earlier measured data that have been published in Refs. [14] and [15], the COR of inelastic impact is mainly dependent upon conditions like collision velocity, mass ratio, material properties, and geometry of the impactors. In order to account for the velocity-dependent characteristic of inelastic impact, Hunt and Crossley [16] developed a nonlinear damping model based on the Kelvin–Voigt viscoelastic model to interpret the COR in vibro-impact.

This paper utilizes the centralized impact dampers and torsional dampers to attenuate lateral vibration of the drillstring that operates close to the bending critical speeds and stick-slip torsional vibration within the operating speed range, respectively. The Timoshenko beam FE model, which accounts for shear deformations, is employed, though they may be negligible due to a large ratio of beam length to diameter. Additionally, stress-stiffening effects are included to account for the influences of gravity and axial loading on transverse string stiffness. As previously stated, stick-slip is too complex to perfectly describe by using a single model, therefore both Coulomb and Stribeck torque models are employed to validate the mitigation effects of the impact and torsional dampers. The pinned-pinned DC span model used in Refs. [10] and [11] is applied for analysis of pure lateral vibrations with impactors. Furthermore, a complete drillstring system (Fig. 1) that is composed of a DP, a DC, a DB, and the impactors and torsional damper installed in the DC is modeled for investigation of working conditions like ROB and DA. The vibro-impact model developed in Ref. [16] is employed to simulate the translational collision between the DC and impactor, and the tangential friction in between is also taken into account. The destabilizing forces induced by drilling fluid or mud are introduced to investigate the stabilizing effects of the impact damper on the drillstring. The torsional damper installed at the bottom of the DC is designed for mitigating stick-slip vibration. In order to provide guidance for acquiring stronger suppression effects on the drillstring vibration, various design parameters of the impactors and torsional damper are analyzed and compared.

Theory

The dynamic formulation based on the Timoshenko beam FEs for the model of a drillstring either in or out of impacting is given as

$$[\mathbf{M}^{e}]\{\ddot{\mathbf{q}}^{e}\} + ([\mathbf{C}^{e}] + [\mathbf{G}^{e}])\{\dot{\mathbf{q}}^{e}\} + ([\mathbf{K}_{s}^{e}] + [\mathbf{K}_{\sigma}^{e}])\{\mathbf{q}^{e}\} = \{\mathbf{f}^{e}\} \quad (1)$$

where the gyroscopic matrix $[G^e]$ is provided in Ref. [17], and the formulation of the remaining terms can be found in Ref. [18]. The stress-stiffening matrix $[K_\sigma^e]$ is representative of the influences of gravity and axial loading on transverse stiffness of the drillstring.

Fig. 2 Cross section of the impact damper and DC at moment of impact

The weight of the drillstring with the impactors and torsional damper and the WOB is accounted for as axial load in the external load vector $\{f^e\}$. Stress stiffening acts to increase lateral bending stiffness under tensile load or reduce it under compressive load.

An impactor collides with the inner surface of the DC when the clearance between them drops to zero. In accordance with the Hertz law of contact, impact forces can be formulated by the force—interference relations (Fig. 2)

$$F = k\delta^{3/2} \tag{2}$$

where F and δ denote the force and interference in contact, respectively, and k is interpreted in the Appendix. As noted in Ref. [16], this formula is only applicable if the dimensions of the impact area are relatively small compared to the radii of curvature of the contact bodies. The size of the impacting bodies in this paper meets this requirement. The shape of the impact damper and DC at the moment of impact can be approximated as sphere and cylindrical cup, respectively.

By referring to Ref. [16], the COR $e_{\rm COR}$ for most materials within a linear elastic range and below the input impact velocity of $0.5\,\rm m/s$ can be written as

$$e_{\rm COR} = 1 - \alpha v_i \tag{3}$$

where α ranges between 0.1 and 0.6 s/m for steel and iron according to Ref. [14], and ν_i refers to the relative velocity of impact (i.e., the input impact velocity shown in Fig. 2). The force–interference law yields the final equation of motion during impacting [16]

$$m_I \ddot{\delta} + c \dot{\delta} + k \delta^{3/2} = 0 \tag{4}$$

where $c = (3/2)\alpha k\delta^{3/2}$. Consequently, the contact forces reacting on the DC are equal to $c\dot{\delta} + k\delta^{3/2}$.

For each pair of impactor and DC section that come into collision, the total transverse loads acting on the DC section are included in the planar impacting model, which is depicted in Fig. 3. The dash line connecting the DC center D and the impactor center I is extended across the contact point Q of the DC and the point P of the impactor. The impactor collides with the DC wall when the distance between D and I, d, exceeds the clearance C_0 , and the collision is approximated to occur in the YZ plane. During the collision, the restoring forces due to the elastic deformation will induce friction forces in the tangential direction, and it is assumed here that only sliding frictions exist between the two impacting surfaces. As shown in Fig. 3, the velocity vectors of the DC and impactor centers are defined as \mathbf{v}_D and \mathbf{v}_I , respectively.

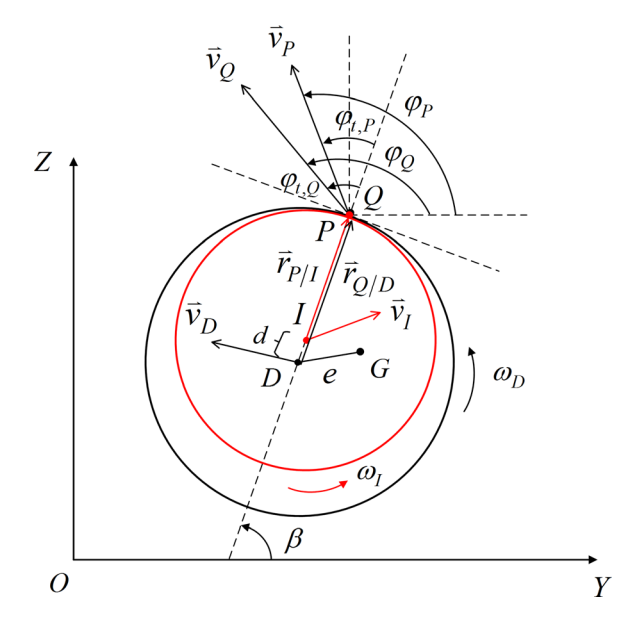


Fig. 3 Planar impacting model for impactor-DC collision

The edge velocity vectors \mathbf{v}_P and \mathbf{v}_Q of the contact points P and Q are derived from

$$\mathbf{v}_P = \mathbf{v}_I + \mathbf{\omega}_I \times \mathbf{r}_{P/I} \tag{5}$$

$$\mathbf{v}_O = \mathbf{v}_D + \mathbf{\omega}_D \times \mathbf{r}_{O/D} \tag{6}$$

baded from http://asmedigitalcollection.asme.org/vibrationaccoustics/article-pdf/138/5051013/6348626/vib_138_05_051013.pdf?casa_token=ZnXLgGMCuO0AAAAA:H_FV1dJJPCfR5pw5NmWoUKXW-R_Wg21Qh-5Ae3Dbf5ypJdy0r1NTmM_dO0lkZaulWpoGb-f2 by Texas A & M University user on 08 Augure

where ω_D and ω_I are the rotation speed vectors of the DC and impactor, respectively, and $\mathbf{r}_{P/I}$ represents the radius vector starting from I and ending at P, and it is similar with $\mathbf{r}_{Q/D}$. The velocity vector angle φ_P can be derived from \mathbf{v}_P , and then, the tangential angle $\varphi_{t,P}$ is obtained from $\varphi_{t,P} = \varphi_P - \beta$, where $\beta = \tan^{-1}((z_I - z_D)/(y_I - y_D))$. $\varphi_{t,Q}$ can be derived in the same way. Finally, the tangential velocities of the contact points P and Q are given as

$$v_{t,P} = v_P \sin\left(\varphi_{t,P}\right) \tag{7}$$

$$v_{t,Q} = v_Q \sin(\varphi_{t,Q}) \tag{8}$$

 δ is related to C_0 by

$$\delta = \sqrt{(y_I - y_D)^2 + (z_I - z_D)^2} - C_0 \tag{9}$$

and the corresponding velocity vector is written as

$$\dot{\boldsymbol{\delta}} = (\dot{y}_I - \dot{y}_D)\mathbf{i} + (\dot{z}_I - \dot{z}_D)\mathbf{j} \tag{10}$$

where **i** and **j** represent the unit vectors in Y and Z directions, respectively, and the vector angle of $\dot{\delta}$ can be subsequently expressed as $\beta_c = \tan^{-1}((\dot{z}_I - \dot{z}_D)/(\dot{y}_I - \dot{y}_D))$. An imbalance mass is located in the middle of the DC (Fig. 1)

An imbalance mass is located in the middle of the DC (Fig. 1) with an eccentric distance e. The drillstring rotation creates centrifugal forces that can be decomposed into two components in Y and Z directions as

$$F_{e,y} = m_D e \omega_D^2 \cos(\omega_D t) \tag{11}$$

$$F_{e,z} = m_D e \omega_D^2 \sin(\omega_D t) \tag{12}$$

The final equations for the impact forces and moments acting on the DC and impactor are given as

$$F_{D,y} = F_{e,y} + k\delta^{3/2}\cos(\beta) + c\dot{\delta}\cos(\beta_c) - \left[k\delta^{3/2} + c\dot{\delta}\cos(\beta - \beta_c)\right]\mu\cos\left(\beta + \frac{\pi}{2}\right) \cdot \operatorname{sign}(\nu_{t,Q} - \nu_{t,P})$$
(13)

$$F_{D,z} = F_{e,z} + k\delta^{3/2}\sin(\beta) + c\dot{\delta}\sin(\beta_c) - \left[k\delta^{3/2} + c\dot{\delta}\cos(\beta - \beta_c)\right]\mu\sin(\beta + \frac{\pi}{2})\cdot\operatorname{sign}(\nu_{t,Q} - \nu_{t,P})$$
(14)

$$T_{D,\varphi} = -r_D \mu [k\delta^{3/2} + c\dot{\delta}\cos(\beta - \beta_c)] \cdot \operatorname{sign}(v_{t,Q} - v_{t,P})$$
 (15)

$$F_{I,y} = -k\delta^{3/2}\cos(\beta) - c\dot{\delta}\cos(\beta_c) + \left[k\delta^{3/2} + c\dot{\delta}\cos(\beta - \beta_c)\right]\mu\cos\left(\beta + \frac{\pi}{2}\right) \cdot \text{sign}(\nu_{t,Q} - \nu_{t,P})$$
(16)

$$F_{I,z} = -k\delta^{3/2}\sin(\beta) - c\dot{\delta}\sin(\beta_c) + \left[k\delta^{3/2} + c\dot{\delta}\cos(\beta - \beta_c)\right]\mu\sin(\beta + \frac{\pi}{2})\cdot\operatorname{sign}(\nu_{t,Q} - \nu_{t,P})$$
(17)

$$T_{I,\varphi} = r_I \mu [k \delta^{3/2} + c \dot{\delta} \cos (\beta - \beta_c)] \cdot \operatorname{sign}(v_{t,Q} - v_{t,P})$$
 (18)

The equations of motion for the impactor may be written as

$$m_I \ddot{y}_I = F_{I,y} \tag{19}$$

$$m_I \ddot{z}_I = F_{I,z} \tag{20}$$

$$J_I \ddot{\varphi}_I = T_{I,\varphi} \tag{21}$$

As demonstrated in Fig. 1, a torsional damper of a cylindrical shape is installed inside the DC. Damping forces may be induced by the drilling mud passing through the outer surface of the torsional damper that has a relative rotational speed with respect to the DC. Larger damping forces can be obtained by encasing the torsional damper surrounded by high-viscosity fluid. Another way to increase the torsional damping is to reduce the clearance between the surfaces of the torsional damper and the DC wall.

In the previous study of stick–slip vibration, either Coulomb [1,3] or Stribeck [7,8] torque model has been applied, but it highly depends on the type of DBs and drilling conditions to decide which torque model is adequate. Therefore, we apply both Coulomb torque T_C and Stribeck torque T_S as TOB to the DB node (the bottom node of the drillstring beam FE model shown in Fig. 1). As illustrated in Fig. 4, the torque T_C equals $T_{\rm stt}$ when the angular velocity of the bit $\omega_B=0$ while it turns into $T_{\rm sld}$ when the bit starts rotating.

In contrast, the Stribeck torque model shown in Fig. 5 allows a continuous change of the TOB with the angular velocity of the bit, which can be described by

$$T_S = -\frac{T_{S0}}{1 + \lambda |\omega_B|} \cdot \operatorname{sign}(\omega_B)$$
 (22)

where a small λ indicates a moderately declining torque curve.

The torsional damper is supported at the bottom of the DC, and damping forces act as torque on the torsional damper. The total angular motion can be described by

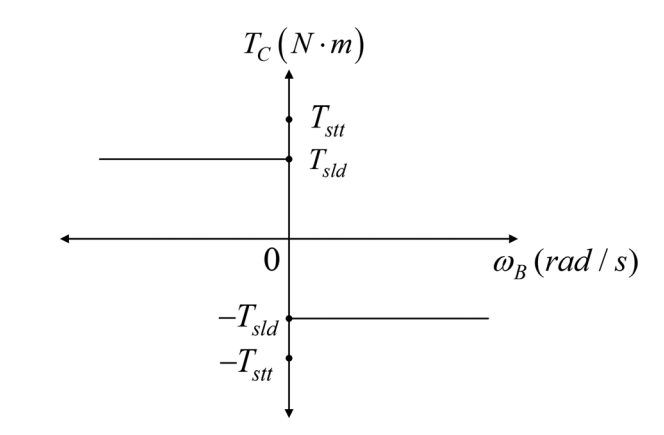


Fig. 4 Coulomb torque model: sliding torque $T_{\rm sld}$ and static torque $T_{\rm stt}$

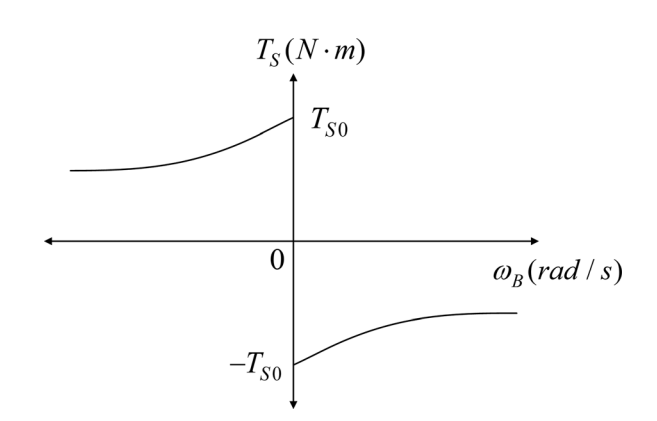


Fig. 5 Stribeck torque model

$$J_A \ddot{\varphi}_A + c_M (\dot{\varphi}_A - \dot{\varphi}_B) + T_A \cdot \text{sign}(\dot{\varphi}_A - \dot{\varphi}_B) = 0$$
 (23)

baded from http://asmedigitalcollection.asme.org/vibrationaccoustics/article-pdf/138/5051013/6348626/vib_138_05_051013.pdf?casa_token=ZnXLgGMCuO0AAAAA:H_FV1dJJPCfR5pw5NmWoUKXW-R_Wg21Qh-5Ae3Dbf5ypJdy0r1NTmM_dO0lkZaulWpoGb-f2 by Texas A & M University user on 08 Augure

where c_M denotes the coefficient of the mud damping, and the torque T_A is induced by sliding frictions between the torsional damper A and inner base of the DC B.

In impacting, the external load $\{f^e\}$ in Eq. (1) consists of the weight of the drillstring with the impactors and torsional damper and the WOB F_W , the TOB T_{TOB} , the impact-induced forces $F_{D,y}$ and $F_{D,z}$ and torque $T_{D,\phi}$ (refer to Eqs. (13)–(18)), and the torque resulting from mud damping $c_M(\dot{\varphi}_A - \dot{\varphi}_B)$ and sliding friction $T_A \cdot \text{sign}(\dot{\varphi}_A - \dot{\varphi}_B)$ (refer to Eq. (23)). The resultant external load vector for the element node n may be written as

$$\{\mathbf{f}_{n}^{e}\} = [F_{W}, F_{D,y}, F_{D,z}, (T_{D,\varphi} + T_{TOB} + c_{M}(\dot{\varphi}_{A} - \dot{\varphi}_{B}) + T_{A} \cdot \operatorname{sign}(\dot{\varphi}_{A} - \dot{\varphi}_{B})), 0, 0]^{T}$$
(24)

The specific load to be added into Eq. (24) depends upon the load condition, and thereby, not all the external loads need to be included. The novel impact and torsional dampers presented here are explained by analysis and demonstrated by simulations, with an underlying assumption that the physical implementations are feasible.

Modeling

The conceptual design of the drillstring that is composed of a DP, a DC, a DB, and the impactors and torsional damper is demonstrated in Fig. 1. The ROB and DA are the working conditions that are commonly seen in a drilling process. It is therefore

Table 1 Parameters of the drillstring

Component	Parameter	Value	Unit
DP	Length	80	m
	OD	100	mm
	ID	75	mm
	Number of beam FEs	40	_
	Density	8000	kg/m ³
	Mass	2199	kg
	Modulus of elasticity	2.1×10^{11}	N/m ²
	Poisson's ratio	0.3	— .
	Transverse mud damping per axial length	50	N s/m ²
	Torsional mud damping per axial length	0–2	N⋅m s/rad
DC	Length	15	m
	OD	150	mm
	ID	75	mm
	Number of beam FEs	10	_
	Density	8000	kg/m ³
	Mass	1590	kg
	Eccentricity	1-8	mm
	Modulus of elasticity	2.1×10^{11}	N/m^2
	Poisson's ratio	0.3	_
	Transverse mud damping per axial length	300	N s/m ²
	Torsional mud damping per axial length	0–6	N⋅m s/rad
Impact damper	Density	8000	kg/m ³
	Number	9	_
	Total mass	143-286	kg
	Modulus of elasticity	2.1×10^{11}	N/m^2
	Poisson's ratio	0.3	_
	Clearance between the impactor and DC	10-30	mm
	Sliding friction coefficient between the impactor and DC	0.4	_
Torsional damper	Length	2.5-6	m
	Density	8000	kg/m ³
	Mass	226-542	kg
	Moment of inertia	0.4-0.8	kg/m ²
	Number	1	_
	Sliding friction coefficient between the torsional damper and inner base of the DC	0.002-0.35	
	Torsional damping	0.25-8	N⋅m s/rad

necessary to ensure the effectiveness of the impactors and torsional damper in these conditions. The parameters of the drill-string system are illustrated in Table 1, and boundary conditions are specified for each working condition.

As the drillstring is fully suspended in the ROB condition and partially suspended in the DA condition, the weight of the impactors and torsional damper will increase the bending stiffness of the drillstring, thereby shifting the critical speeds. To exclude the influence of shifting critical speeds on the vibration amplitude, the weight of the impactors and torsional damper is always accounted for in the comparison of vibrations at the critical speed even if there are no dampers in the drillstring.

The length of the DP varies with the depth of the well and may even reach a few kilometers. In contrast, the diameter of the DP is normally less than 0.2m, which makes the DP act more like a string. Eighty meters is enough long for the investigation of the influences of the impact dampers on the lateral string vibrations. With regard to the length and diameter of the DC, it is similar to the DP, i.e., slender as a string, except that the DC is usually 27-36 m in length. Two or more stabilizers are installed on the DC, and the segment between two stabilizers (called DC span) is about 15m long. The DC may consist of several DC spans, and the total length of the DC is dependent on the BHA design. According to Refs. [10] and [11], the lateral position of the stabilizer is assumed constrained to zero, and the first bending mode is most commonly seen within the rotating speed range of the drillstring. Therefore, it is acceptable for a conceptual design to use a DC span with two stabilizers located at both ends (see pinned points A and B shown in Fig. 1) to investigate the lateral dynamics of the DC in impacting.

ROB. The drillstring while rotating off bottom can be modeled by setting both pinned points A and B in Fig. 1 free, analogous to a pendulum with the top end O pinned. The boundary conditions may be written as $x_O = y_O = z_O = 0$ and $\omega_O = \text{const.}$, where the subscript O denotes the top end of the DP near the hoist/rotary table, and the spin speed of the top drive ω_O is constant. It is assumed that the DC mass is eccentric, and no drilling torque acts on the DB. The drillstring carries the tensile axial load resulting from the weight of the DP, DC, impactors, and torsional damper.

DA. With regard to the DA condition, both ends (*A* and *B*) of the DC shown in Fig. 1 are pinned, and the drilling torque acting on the DB is included. Hence, the boundary conditions may be written as $x_O = y_O = z_O = 0$, $\omega_O = \text{const.}$, and $y_A = z_A = y_B = z_B = 0$. In the axial direction, the hoist pulls the DP, and the bottom of the borehole supports the DC weight. That is to say, the DP is in tension, and the DC is under compressive load. The unbalanced forces caused by the eccentric DC mass are loaded in the middle of the DC.

Simulation Results

ROB. The drillstring operating in the ROB condition has been simulated, and the results are demonstrated in Figs. 6–13. As Fig. 6 shows, the largest lateral deflections of the DC in the whirl mode at the bending critical speed of $\Omega = 119 \, \text{rpm}$ are located at two bending peaks, i.e., point C (4.5 m away from point A) and point B (the bottom of the DC).

The impactors are installed in the DC in such a way that the mass of nine impactors is equally distributed (31.8 kg per element,

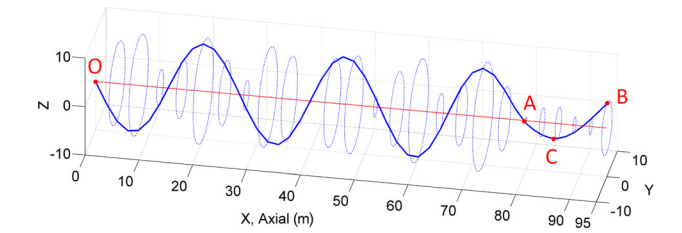


Fig. 6 Mode shape of the drillstring at the bending critical speed of $\Omega =$ 119 rpm

286 kg in total) with a clearance of $d=10\,\mathrm{mm}$ between the impactor and DC. As a result, the vibration amplitudes of points B and C at $\Omega=119\,\mathrm{rpm}$ are reduced from 22 mm and 12 mm to 14 mm and 8 mm, respectively, which can be seen from Figs. 8 and 9. This suppression effects on the vibration amplitudes are attributed to the impacting between the DC and impactors that may dissipate the kinetic energy of the drillstring. If we reduce the mass of the impactors from 286 kg (18% of the mass of the DC) to 143 kg (9% of the mass of the DC), in which case the mode shape of the drillstring is the same as that shown in Fig. 6, the vibration amplitudes at B and C increase from 14 mm and 8 mm to 16 mm and 9 mm, respectively, which is displayed in Figs. 8–10. This increase can be understood by looking into either the impacting model with the COR or the one with a Hertzian contact force and a nonlinear viscous damping force.

As far as the impacting model with the COR is concerned, the velocity of the DC after inelastic collision can be described by

$$\dot{x}_D^+ = \frac{1}{1+\eta} \left[\eta (1+e_{\rm COR}) \dot{x}_I^- + (1-\eta e_{\rm COR}) \dot{x}_D^- \right] \tag{25}$$
 where \dot{x}_D represents the velocity of the DC, \dot{x}_I the velocity of the

where \dot{x}_D represents the velocity of the DC, \dot{x}_I the velocity of the impactor, η the mass ratio of the impactor to the DC, and the superscripts + and - denote the velocity after and before collision, respectively. If we assume that e_{COR} is constant (if η does not change too much) and $\dot{x}_I^- = 0$, it can be derived from Eq. (25) that \dot{x}_D^+ drops when η rises, which implies that after collision, the kinetic energy of the DC containing the impactors with larger mass is less than with smaller mass. In other words, more kinetic energy is dissipated by the impactor with larger mass than with smaller mass, indicating that the lateral vibration is attenuated to a larger extent. This conclusion is verified by the simulation results presented in Figs. 8–10 that after the mass of the impactors increases, the lateral velocities of points B and C in impacting decrease from 200 mm/s and 115 mm/s to 180 mm/s and 105 mm/s, respectively.

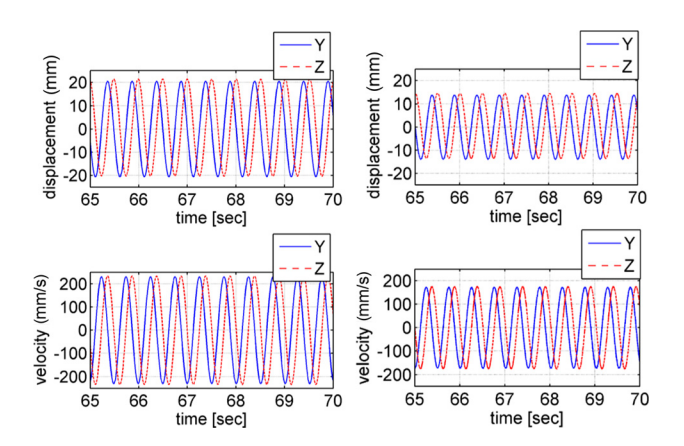


Fig. 7 Displacement and velocity of the DC at point B without (left) or with (right) impactors with $d=10\,\mathrm{mm}$ and the total impactor mass of 286 kg in the ROB condition at the critical speed of $\Omega=119\,\mathrm{rpm}$

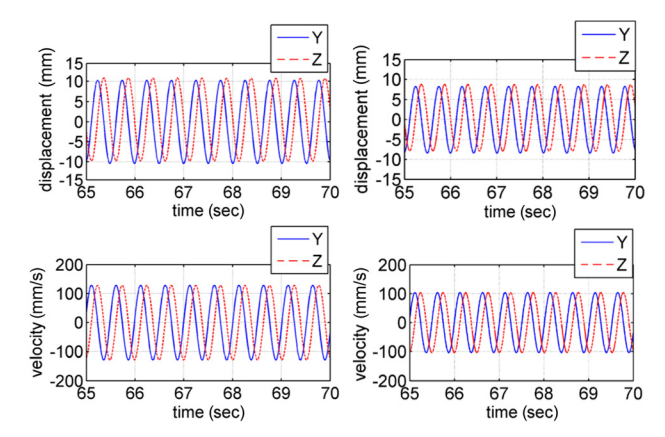


Fig. 8 Displacement and velocity of the DC at point C without (left) or with (right) impactors with $d=10\,\mathrm{mm}$ and the total impactor mass of 286 kg in the ROB condition at the critical speed of $\Omega=119\,\mathrm{rpm}$

Regarding the impacting model with a Hertzian contact restoring force and a nonlinear viscous contact damping force, the enhancement of the vibration suppression is attributed to the larger inertia of the impactors, which renders less change of the velocities of the impactors. In other words, the impactor does not follow the motion of the DC under contact forces, implying that the relative velocity between the impactor and the DC may increase (this conclusion does not apply to the impactor with much smaller mass than the DC). According to Eq. (3), an increase in the relative input velocity v_i yields a smaller COR, thereby dissipating more kinetic energy of the DC. As demonstrated in Fig. 11, the velocity of the impactor with respect to point C under the total impactor mass of 286 kg is a little larger than under the total impactor mass of 143 kg. In addition to v_i , the coefficient α usually increases with the mass of the impactor according to the measured data presented in Ref. [14]. Hence, it can be clearly seen that a larger impactor mass renders an increase in both v_i and α , thereby causing the COR to decline and leading to more dissipation of kinetic energy of the DC.

Moreover, the clearance between the impactor and DC also has an effect on the suppression of lateral vibrations. As can be seen from Fig. 12, the vibration reduction is greater with $d=20\,\mathrm{mm}$ than with $d=30\,\mathrm{mm}$. The collision state shown in Fig. 13 corresponds to a total impactor mass of 286 kg in the ROB condition at $\Omega=119$ rpm. This plot indicates that the impactor collides with the DC more frequently with $d=20\,\mathrm{mm}$ than with $d=30\,\mathrm{mm}$. Thus, the greater vibration reduction may be plausibly explained

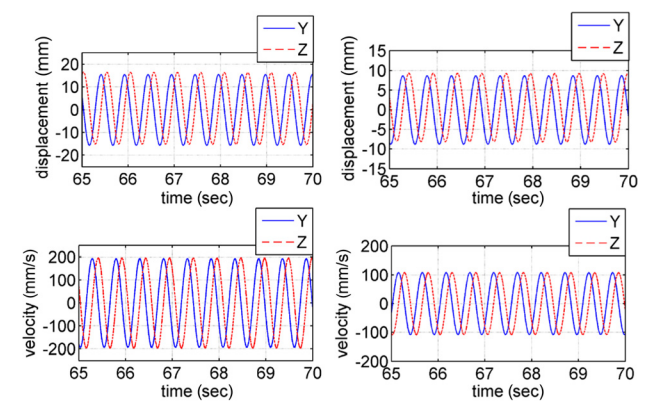


Fig. 9 Displacement and velocity of the DC at point B (left) and point C (right) with $d=10\,\mathrm{mm}$ and the total impactor mass of 143 kg under impacting in the ROB condition at the critical speed of $\Omega=117\,\mathrm{rpm}$

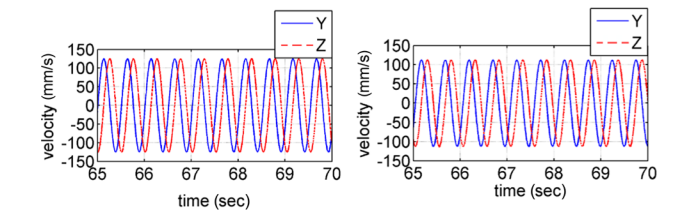


Fig. 10 Velocity of the impactor with respect to the DC at point C with d=10 mm and the total impactor mass of 286 kg (left) at the critical speed of $\Omega=119$ rpm or 143 kg (right) at the critical speed of $\Omega=117$ rpm under impacting in the ROB condition

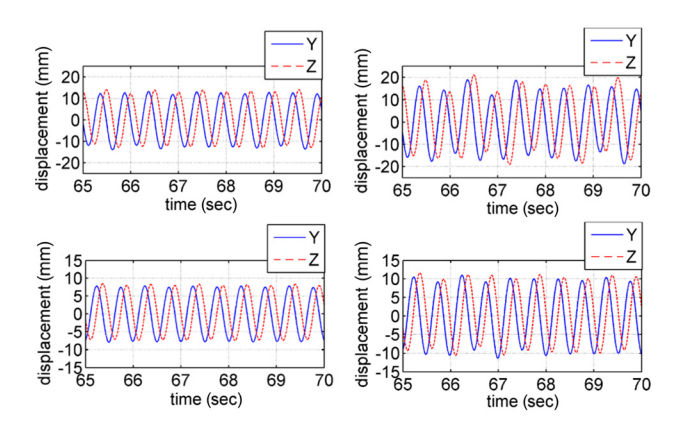


Fig. 11 Displacement of the DC at point B (top) and point C (bottom) with $d=20\,\mathrm{mm}$ (left) or $d=30\,\mathrm{mm}$ (right) and the total impactor mass of 286 kg under impacting in the ROB condition at the critical speed of $\Omega=119\,\mathrm{rpm}$

by the smaller clearance instigating more frequent impacting, which leads to increased dissipation of kinetic energy.

The energy dissipation mechanism is more complex though since a smaller clearance is likely to cause a decrease in the relative impact velocity as the impact damper may closely follow the DC with a small clearance. This conclusion is verified by analyzing the orbits of the impactor, which is presented as the relative displacements of the impactor with respect to the DC in Fig. 13. It can be seen from these orbits that the impactor follows the DC more closely under $d=20\,\mathrm{mm}$ than under $d=30\,\mathrm{mm}$. According to Eq. (3), the COR will increase when the input impact velocity drops. Hence, the frequent impacting caused by a small clearance may not necessarily increase the total amount of dissipated kinetic energy. This is illustrated in Fig. 7, which shows that the impactor

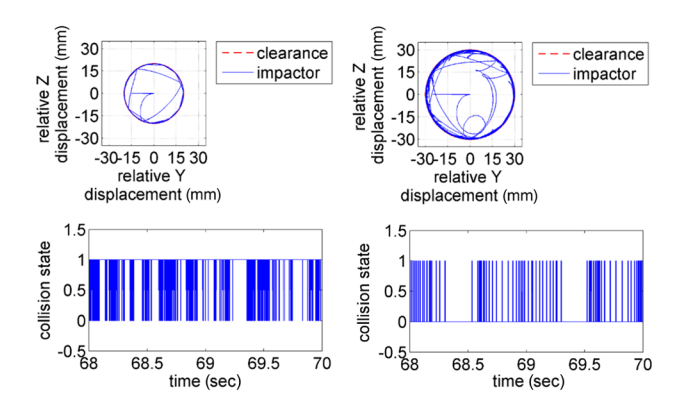


Fig. 12 Orbit of the relative displacement of the impactor with respect to the DC (top) and collision state (1 represents collision and 0 no collision) between the impactor and the DC (bottom) at point C with $d = 20 \, \text{mm}$ (left) or $d = 30 \, \text{mm}$ (right)

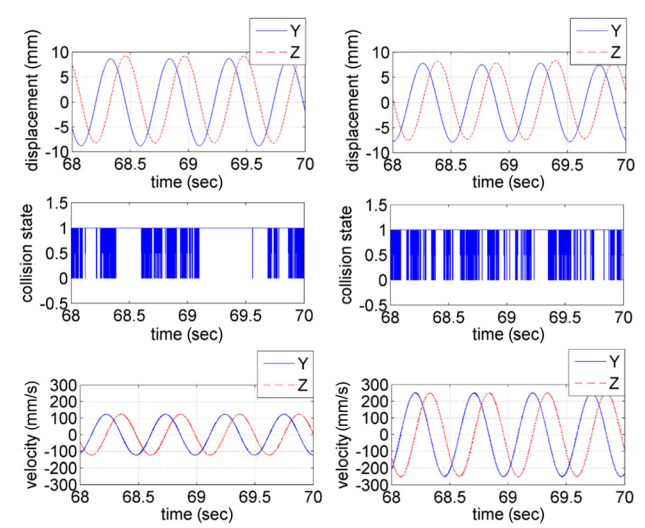


Fig. 13 Displacement of the DC (top), collision state (1 represents collision and 0 no collision) between the impactor and DC (middle), and velocity of the impactor with respect to the DC (bottom) at point C with $d=10\,\mathrm{mm}$ (left) or $d=20\,\mathrm{mm}$ (right) and the total impactor mass of 286 kg in the ROB condition at the critical speed of $\Omega=119\,\mathrm{rpm}$

collides with the DC more frequently with $d=10\,\mathrm{mm}$ than with $d=20\,\mathrm{mm}$, but the impacting velocity, i.e., the velocity of the impactor with respect to the DC, is smaller under $d=10\,\mathrm{mm}$ than under $d=20\,\mathrm{mm}$. Due to this, the vibration amplitudes of the DC at point C with $d=10\,\mathrm{mm}$ are larger than that with $d=20\,\mathrm{mm}$.

DA. The drillstring may undergo both lateral whirl and torsional stick-slip vibrations while drilling ahead. As shown in Fig. 14, the DC mode that corresponds to the bending critical speed of $\Omega = 91 \text{ rpm}$ is the first bending mode with the largest deflection (point D) appearing in the middle of the DC. The simulation results of the drillstring vibration utilizing the Coulomb torque model with $T_{\rm sld} = 0.8T_{\rm stt}$ are demonstrated in Fig. 15. Like in the ROB condition, the weight of the impactors and torsional damper in the DA condition is included regardless of impacting, and the total mass of the impactors is 286 kg (18% of the mass of the DC). It can be seen from Fig. 15 that the largest vibration amplitude approaches 14 mm without the impactors and torsional damper and drops to 7 mm in impacting, and the stick-slip vibrations dampened out owing to the torsional damper. For the case presented in Fig. 15, nine impactors are installed in an even mass distribution in the DC (31.8 kg per element of the DC). The mass and the moment of inertia of the torsional damper are 226 kg (14% of the mass of the DC) and 0.4 kg/m^2 , respectively.

In addition, the mass distribution of the impactors may have influences on the suppression effects. The mass of the impactors in the DA condition is distributed as (15.9, 15.9, 31.8, 47.7, 63.6, 47.7, 31.8, 15.9, and 15.9) kg, which is proportional to the displacement distribution of the DC in the first bending mode (Fig. 14), for the nine impactors instead of 31.8 kg for each

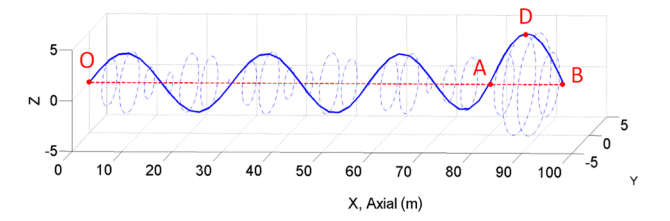


Fig. 14 Mode shape of the drillstring at the bending critical speed of $\Omega=$ 91 rpm



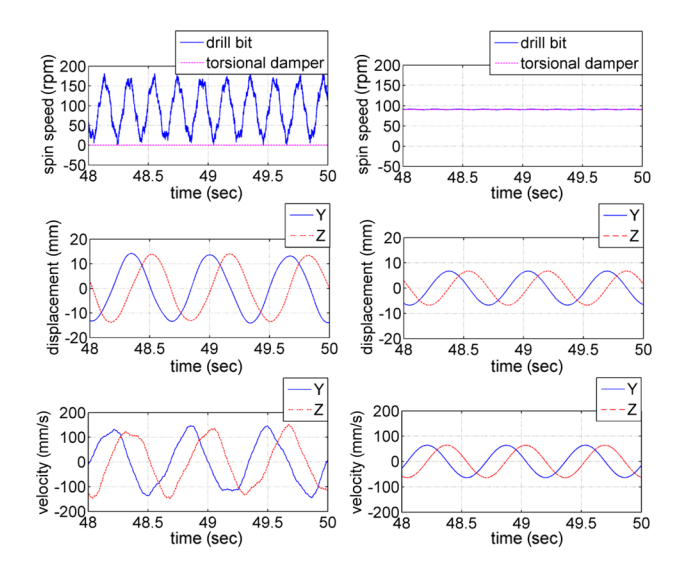


Fig. 15 Rotary speed of the DB, lateral displacement and velocity of the DC at point D utilizing the Coulomb torque model without (left) or with (right) the impactors and torsional damper under d=10 mm, and the even mass distribution of the impactors in the DA condition at the critical speed of $\Omega=91$ rpm

impactor. For simplicity, we call it the mode-oriented mass distribution. These two ways of mass distribution are compared in Figs. 15 and 16. The simulation results show that a larger mass distributed at point D (the location of the largest displacement in the bending mode) leads to a larger reduction of the vibration amplitude, which is further reduced from 7 mm (Fig. 15) to 4 mm (Fig. 16). The reason for this larger reduction is partially the same as what has been clarified in the ROB condition, i.e., that the impactor with a larger mass (63.6 kg) is able to dissipate more kinetic energy of the DC than with a smaller mass (31.8 kg). The difference lies in that the total mass of the impactors utilizing the mode-oriented distribution remains constant (286 kg), compared to increasing the mass of the impactors in the ROB case. That is to say, the mode-oriented mass distribution is able to enhance the suppression effects on the lateral vibrations of the DC without changing the total mass of the impactors.

The stick-slip could appear at a wide range of rotary speeds. As displayed in Fig. 15, the peak rotary speed of the DB in the stick-slip vibration may reach twice the rotary speed of the top drive, thereby aggravating the whirl vibration of the DC. Ideally, a torsional damper is installed inside the DC to mitigate the stick-slip vibration of the drillstring, and the torsional damper with a larger moment of inertia is more effective than with a smaller moment of inertia. In practice, however, the torsional damper may be less effective due to the sliding friction torque between the torsional damper and the inner base of the DC that supports the weight of the torsional damper. For the simulation results demonstrated in Figs. 15 and 16, the coefficients of sliding friction between the torsional damper and inner base of the DC are both set as $\mu_A = 0.002$, which is close to the coefficient of rolling friction for an angular contact thrust ball bearing. Similar to the drillstring utilizing the Coulomb torque model, the stick-slip vibration induced by the Stribeck torque model can be completely attenuated by the torsional damper under a small coefficient of friction like $\mu_A = 0.002$, which is demonstrated in Fig. 17.

It would be simpler for assembly if the torsional damper is installed directly on the inner base of the DC. In this condition, the friction between the torsional damper and DC base may be treated as the sliding friction between two metal surfaces. Normally, the coefficient of dry sliding friction μ_A is close to 0.35, and μ_A may decrease with the mud fluid lubricating the inner base of the DC. As can be seen from Fig. 18, for the Coulomb torque

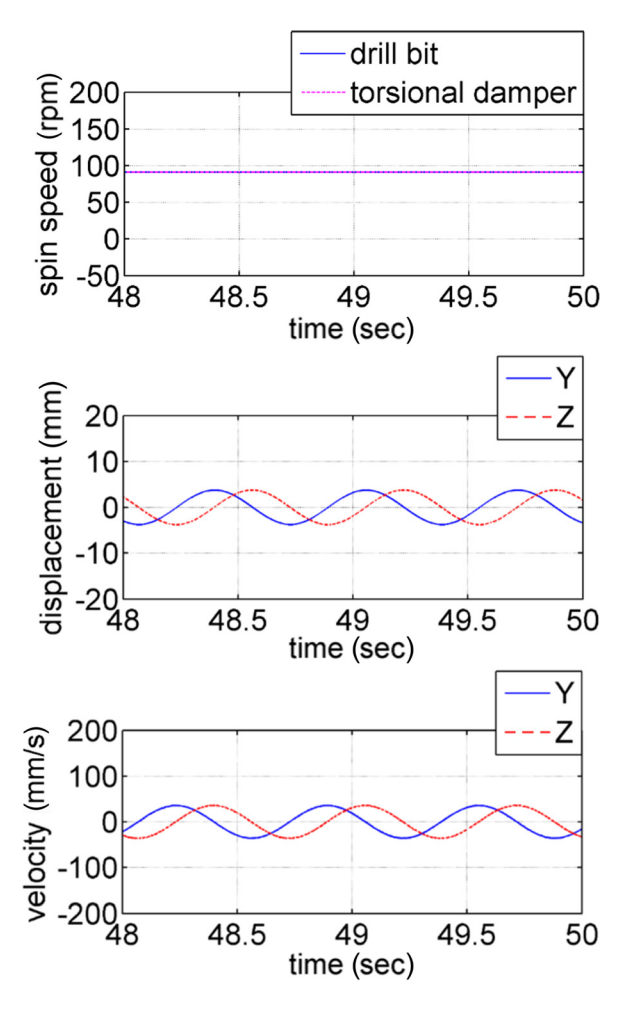


Fig. 16 Rotary speed of the DB, lateral displacement and velocity of the DC at point D utilizing the Coulomb torque model with the impactors and torsional damper under $d=10\,\mathrm{mm}$, and the mode-oriented mass distribution of the impactors in the DA condition at the critical speed of $\Omega=91\,\mathrm{rpm}$

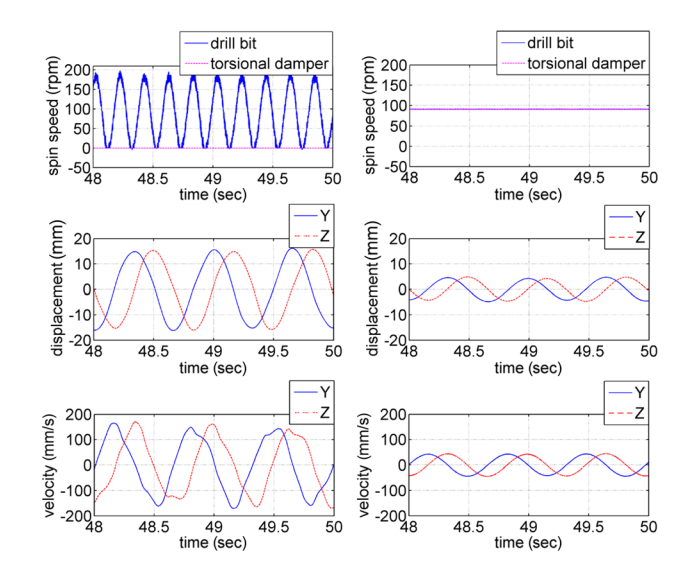


Fig. 17 Rotary speed of the DB, lateral displacement and velocity of the DC at point D utilizing the Stribeck torque model without (left) or with (right) the impactors and torsional damper under $d=20\,\mathrm{mm}$, and the mode-oriented mass distribution of the impactors in the DA condition at the critical speed of $\Omega=91\,\mathrm{rpm}$

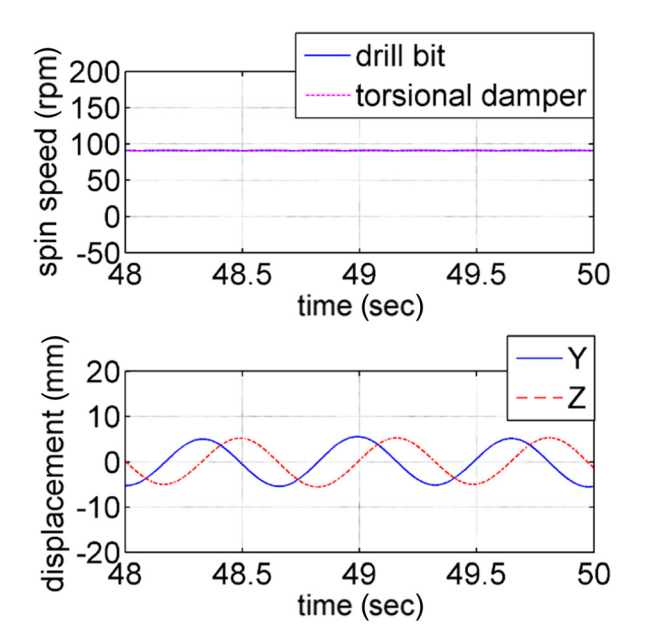


Fig. 18 Rotary speed of the DB and lateral displacement of the DC at point D utilizing the Coulomb torque model with the impactors and torsional damper under $d=10\,\mathrm{mm},~\mu_A=0.35,$ and the even mass distribution of the impactors in the DA condition at the critical speed of $\Omega=91\,\mathrm{rpm}$

model, an increase in the friction torque between the torsional damper and inner base of the DC results only in a very minor reduction in stick-slip vibration mitigation. On the contrary, as shown in Fig. 19, the torsional vibration of the drillstring that utilizes the Stribeck torque model with $\lambda = 0.02$ may result in limit cycles with the amplitudes oscillating between 77 rpm and 105 rpm under a large coefficient of friction of $\mu_A = 0.35$. The limit cycles may dampen out under either a small μ_{A} or a moderately declining torque curve with $\lambda < 0.02$. This is because a large friction torque, which is attributed to a large μ_A , makes the torsional damper closely chase, or drive the rotating DC. In other words, the relative rotating speed between the torsional damper and DC approaches zero, resulting in less dissipation of kinetic energy. Therefore, any support structure with a low friction torque, such as an angular contact thrust ball bearing, is useful in enhancing the mitigation effects on torsional vibrations. The Stribeck torque model has the characteristic that torque decreases with increased rotary speed, which induces a negative damping and may cause severe torsional vibrations. A moderately declining torque curve, which implies a small λ , leads to a small negative damping. In accordance with Ref. [7], the torque curve usually declines mildly in practice, indicating that $\lambda < 0.025$ is adequate for the real DA case.

In comparison with the higher-frequency stick–slips shown in Figs. 15 and 17, oscillations at the first torsional mode of the full drillstring with a period of $2-10\,\mathrm{s}$ are usually more damaging. To model these lower natural frequencies, the length of the DP is extended to 1.2 km, and the DC to 30 m. Additionally, the external torsional damping caused by mud and drilling fluid is set to zero in order to exclude its influence on the mitigation of stick–slip vibrations. Zero torsional damping may result in severe speed oscillation. The speed oscillation will increase as WOB increases so the parametric study starts at zero WOB. The simulation results are presented in Figs. 20 and 21. For the Coulomb torque model, as is shown in Fig. 20, the torsional vibration of the DB under the extended 30 kN WOB is suppressed by the torsional damper in the simple speed oscillation period. In contrast, the highest WOB to extend for the Stribeck torque model (Fig. 21) is 3 kN.

Besides the stick-slip, the DC and DB may be destabilized by mud or drilling fluid. As pointed out in Ref. [19], this type

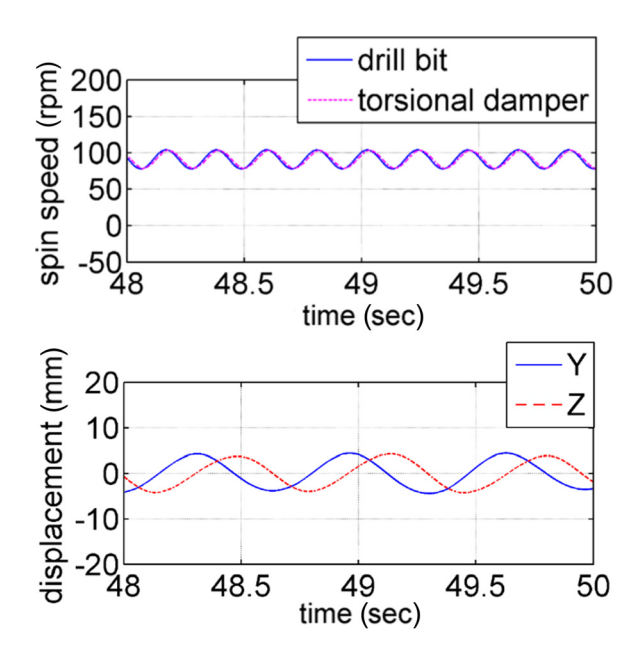


Fig. 19 Rotary speed of the DB and lateral displacement of the DC at point D utilizing the Stribeck torque model with the impactors and torsional damper under $d=20\,\mathrm{mm},~\mu_A=0.35,$ and the mode-oriented mass distribution of the impactors in the DA condition at the critical speed of $\Omega=91\,\mathrm{rpm}$

of destabilizing force may be explained in the presence of cross-coupled stiffness in the form of $\begin{bmatrix} 0 & K_{XY} \\ -K_{XY} & 0 \end{bmatrix}$ at the DC and DB. The simulation results from the drillstring model with $K_{XY} = 7000 \, \text{N/m}$ are demonstrated in Figs. 22 and 23. The eigenvalue of the drillstring system for the first bending mode of the DC is 0.46 + j9.78, indicating a negative damping ratio of $\xi = -0.05$. As can be seen from Fig. 22, the DC without the impactors and torsional damper is unstable, and the amplitudes of lateral vibration reach $400 \, \text{mm}$ in $10 \, \text{s}$, which far exceed the clearance between the DC and the borehole. A short time period of $t = 8 - 10 \, \text{s}$ is selected to clearly present the stick–slip vibration of the DB. When the impactor dampers and torsional damper

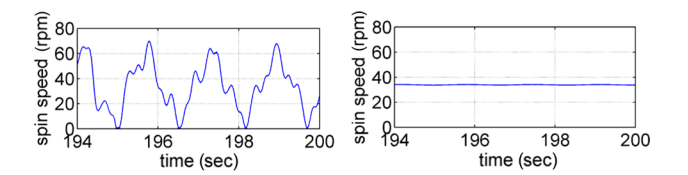


Fig. 20 Rotary speed of the DB utilizing the Coulomb torque model without (left) or with (right) the impactors and torsional damper in the DA condition in the first torsional mode of the drillstring under 30 kN WOB in the first torsional mode at the critical speed of $\Omega=34\,\text{rpm}$

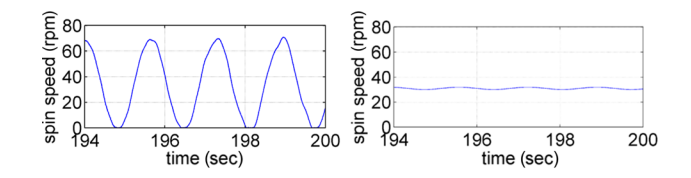


Fig. 21 Rotary speed of the DB utilizing the Stribeck torque model without (left) or with (right) the impactors and torsional damper in the DA condition in the first torsional mode of the drillstring under 3 kN WOB in the first torsional mode at the critical speed of $\Omega=34\,\text{rpm}$

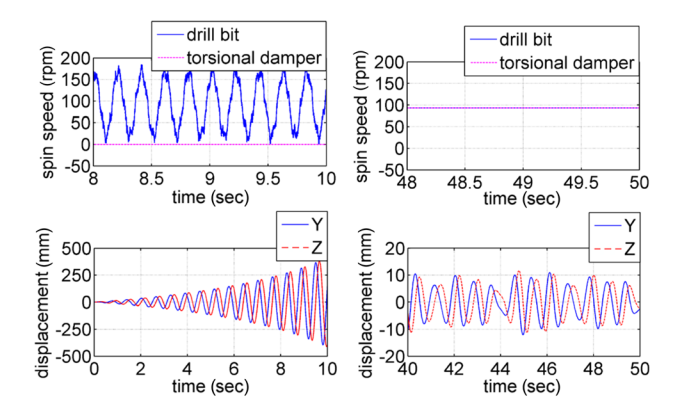


Fig. 22 Rotary speed of the DB and lateral displacement of the DC at point D utilizing the Coulomb torque model without (left) or with (right) the impactors and torsional damper, with cross-coupled stiffness, $d=20\,\mathrm{mm}$ and the mode-oriented mass distribution of the impactors in the DA condition at the critical speed of $\Omega=93\,\mathrm{rpm}$

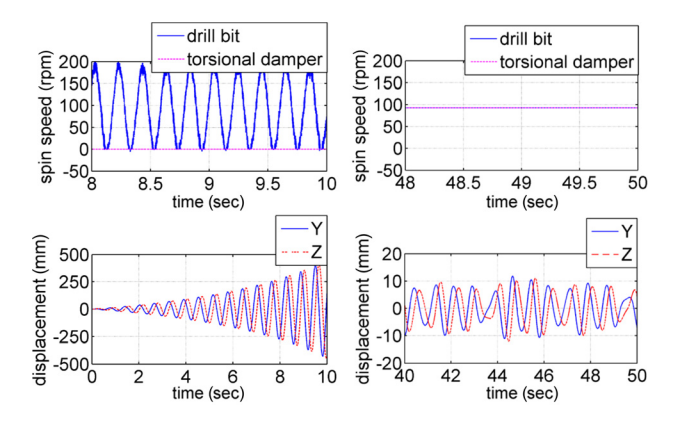


Fig. 23 Rotary speed of the DB and lateral displacement of the DC at point D utilizing the Stribeck torque model without (left) or with (right) the impactors and torsional damper, with cross-coupled stiffness, $d=20\,\mathrm{mm}$ and the mode-oriented mass distribution of the impactors in the DA condition at the critical speed of $\Omega=93\,\mathrm{rpm}$

are installed in the DC, the drillstring becomes stable, and the vibration amplitudes of the DC are attenuated to 12 mm. Furthermore, the stick–slip vibration is completely suppressed. It is similar with the drillstring utilizing the Stribeck torque model that the impact dampers are able to stabilize the drillstring (Fig. 23). Owing to the impactors, the accumulative kinetic energy resulting from the negative damping is dissipated through impacting.

Summary and Conclusions

Impact dampers are offered as an alternative to the conventional viscous fluid and elastomer mechanisms for suppressing lateral whirl vibration of the drillstring that is close to the bending critical speeds. In addition, a torsional damper is introduced to attenuate stick—slip vibration of the DB and tubulars. In order to simulate the collision between the impactor and DC, a vibroimpact model, which includes a nonlinear Hertzian contact restoring force and a viscous contact damping force as the radial impacting forces and considers the sliding frictions in between as tangential forces, is applied. Both Coulomb and Stribeck friction torque models are utilized to simulate torsional stick—slip vibration of the DB. The stress-stiffening effects resulting from the weight of the entire drillstring and the axial loads are accounted for in analysis of lateral vibration.

Regarding the ROB condition, it can be concluded from the simulation results that the larger the mass of the impact dampers

becomes, the more the lateral vibrations of the DB and DC are suppressed. Properly designing the clearance between the impactors and DC is also essential to the suppression effects. The amplitudes of lateral vibration in impacting may drop with a decrease in clearance, however, an excessively small clearance may impede the enhancement of the suppression effects.

In the DA condition, lateral vibration of the DC can be attenuated to a larger extent by the impact dampers with a larger total mass or with a mode-oriented mass distribution, in which case the total mass of the impactors remains constant. Generally, a smaller clearance between the impactor and DC may enhance the mitigation of lateral vibration, however, excessively small clearances will diminish the mitigation.

With regard to stick—slip vibration, the torsional damper with a larger inertia and a lower coefficient of friction between the torsional damper and inner base of the DC is more effective in mitigating stick—slip vibration in both Coulomb and Stribeck friction torque models. The stick—slip vibration (simple speed oscillation) of the DB may be completely dampened by the torsional damper if the coefficient of friction between the torsional damper and inner base of the DC is small. With a large coefficient of friction, the angular velocity of the DB may exhibit limit cycles. In addition, the range of WOB may be extended by using the torsional damper in the speed oscillation period. Finally, a drillstring that is experiencing lateral vibration caused by drilling mud induced, destabilizing, cross-coupled stiffness forces may be stabilized by the impact dampers.

Nomenclature

 c_M = coefficient of damping of the mud

 C_0 = clearance between the DC and impactor

 $\{\mathbf{f}\}$ = external load vector

 $\hat{F} = \text{force}$

j = imaginary unit of a complex number

J =moment of inertia

m = mass

 $[M], [C], [K_S] =$ mass, external damping, and structural stiffness

matrices, respectively

q = translational, rotational, axial, and torsional DOFs

r = radius

sign = signum function

T = torque

 $T_{\rm sld} = {\rm sliding\ torque}$

 $T_{\rm stt} = {\rm static\ torque}$

X, Y, Z =Cartesian coordinates

 $\eta = \text{mass ratio of the impactor to the DC}$

 μ = coefficient of sliding friction between the impact damper and inner wall of the DC

 μ_A = coefficient of friction between the torsional damper and inner base of the DC

 $\xi = \text{damping ratio}$

 $\varphi = \text{rotation angle}$

 $\omega = {
m angular\ velocity}$

 Ω = rotary speed of the drillstring

Subscripts

A =torsional damper

B =bottom of the DC or the DB

e = eccentricity

I,D = impactor and DC, respectively

P,Q =contact point of the impactor and DC, respectively

S = structural stiffness matrix including bending, shear, axial, and torsional stiffness components

t =tangential direction

 $y, z, \varphi = Y, Z$, and torsional directions, respectively

 $\sigma =$ stress stiffness matrix

Superscripts

e = elemental matrix or vector $\cdot =$ derivative with respect to time

Appendix

By referring to Ref. [14], the parameter k in the formula for the force–interference relations can be expressed as

$$k = \frac{4}{3} \cdot \frac{q_k}{(\delta_1 + \delta_2)\sqrt{A + B}} \tag{A1}$$

where

$$\delta_1 = \frac{1 - \nu_1^2}{E_1 \pi} \tag{A2}$$

$$\delta_2 = \frac{1 - \nu_2^2}{E_2 \pi} \tag{A3}$$

 ν and E denote the Poisson's ratio and modulus of elasticity, respectively, and the subscripts 1 and 2 refer to the sphere and cylindrical cup, respectively. For contact between a sphere and a cylindrical cup, A and B can be obtained from

$$A = \frac{1}{2} \left(\frac{1}{R_1} - \frac{1}{R_2} \right) \tag{A4}$$

$$B = \frac{1}{2R_1} \tag{A5}$$

where R_1 and R_2 represent the radius of sphere and cylindrical cup, respectively. q_k is dependent upon A and B and can be referred in Ref. [14].

References

- Jansen, J. D., and van den Steen, L., 1995, "Active Damping of Self-Excited Torsional Vibrations in Oil Well Drillstrings," J. Sound Vib., 179(4), pp. 647–668.
 Sowers, S. F., Dupriest, F. E., Bailey, J. R., and Wang, L., 2009, "Use of Roller
- [2] Sowers, S. F., Dupriest, F. E., Bailey, J. R., and Wang, L., 2009, "Use of Roller Reamers Improve Drilling Performance in Wells Limited by Bit and

- Bottomhole Assembly Vibrations," SPE/IADC Drilling Conference and Exhibition, Amsterdam, The Netherlands, Mar. 17–19, SPE Paper No. 119375-MS, pp. 405–412.
- [3] Kyllingstad, A., and Halsey, G. W., 1988, "A Study of Slip/Stick Motion of the Bit," SPE Drill. Eng., 3(04), pp. 369–373.
- [4] Liao, C.-M., Balachandran, B., Karkoub, M., and Abdel-Magid, Y. L., 2011, "Drill-String Dynamics: Reduced-Order Models and Experimental Studies," ASME J. Vib. Acoust., 133(4), p. 041008.
- ASME J. Vib. Acoust., 133(4), p. 041008. [5] Vlajic, N., Liao, C.-M., Karki, H., and Balachandran, B., 2013, "Draft: Stick-Slip Motions of a Rotor-Stator System," ASME J. Vib. Acoust., 136(2), p. 021005.
- [6] Dawson, R., Lin, Y. Q., and Spanos, P. D., 1987, "Drill String Stick-Slip Oscillations," SEM Spring Conference on Experimental Mechanics, Houston, TX, June 14–19, pp. 590–595.
- [7] Brett, J. F., 1992, "The Genesis of Bit-Induced Torsional Drillstring Vibrations," SPE Drill. Eng., 7(03), pp. 168–174.
- [8] Leine, R. I., van Campen, D. H., and Keultjes, W. J. G., 2002, "Stick-Slip Whirl Interaction in Drillstring Dynamics," ASME J. Vib. Acoust., 124(2), pp. 209–220.
- [9] Jansen, J. D., 1991, "Non-Linear Rotor Dynamics as Applied to Oilwell Drillstring Vibrations," J. Sound Vib., 147(1), pp. 115–135.
- [10] Bailey, J. R., Biediger, E., Sundararaman, S., Carson, A. D., Elks, W. C., and Dupriest, F. E., 2008, "Development and Application of a BHA Vibrations Model," International Petroleum Technology Conference (IPTC), Kuala Lumpur, Malaysia, Dec. 3–5, Paper No. IPTC 12737.
- [11] Bailey, J. R., Elsborg, C. C., James, R. W., Pastusek, P., Prim, M. T., and Watson, W. W., 2013, "Design Evolution of Drilling Tools to Mitigate Vibrations," SPE Drill. Completion, 28(04), pp. 350–369.
- [12] Moore, J. J., Palazzolo, A. B., Gadangi, R., Nale, T. A., Klusman, S. A., Brown, G. V., and Kascak, A. F., 1995, "A Forced Response Analysis and Application of Impact Dampers to Rotordynamic Vibration Suppression in a Cryogenic Environment," ASME J. Vib. Acoust., 117(3A), pp. 300–310.
- [13] McElhaney, J. M., Palazzolo, A., and Kascak, A., 1997, "Modeling and Simulation Methods for MDOF Structures and Rotating Machinery With Impact Dampers," ASME J. Eng. Gas Turbines Power, 119(2), pp. 436–446.
- [14] Goldsmith, W., 1960, Impact: The Theory and Physical Behaviour of Colliding Solids, Edward Arnold, Ltd., London, UK.
- [15] Johnson, K. L., 1985, Contact Mechanics, Cambridge University Press, Cambridge, UK.
- [16] Hunt, K. H., and Crossley, F. R. E., 1975, "Coefficient of Restitution Interpreted as Damping in Vibroimpact," ASME J. Appl. Mech., 42(2), pp. 440–445.
- [17] Nelson, H. D., 1980, "A Finite Rotating Shaft Element Using Timoshenko Beam Theory," ASME J. Mech. Des., 102(4), pp. 793–803.
- [18] Cook, R. D., Malkus, D. S., Plesha, M. E., and Witt, R. J., 2001, Concepts and Applications of Finite Element Analysis, Wiley, New York.
- [19] Childs, D., 1993, Turbomachinery Rotordynamics: Phenomena, Modeling, and Analysis, Wiley, New York.